Direct numerical simulation of fully saturated flow in natural porous media at the pore scale: a comparison of three computational systems

M. Siena[1] · J. D. Hyman[2,4] · M. Riva[1,3] · A. Guadagnini[1,3] · C. L. Winter[3,4] · P. K. Smolarkiewicz[5] · P. Gouze[6] · S. Sadhukhan[6] · F. Inzoli[7] · G. Guédon[7] · E. Colombo[7]

Received: 30 July 2014 / Accepted: 5 April 2015
Published online: 01 May 2015

✉ M. Siena
martina.siena@polimi.it

[1] Dipartimento di Ingegneria Civile e Ambientale, Politecnico di Milano, Milan, 20133, Italy

[2] Earth and Environmental Sciences Division and Theoretical Division, Los Alamos National Laboratory, MS T003, Los Alamos, NM 87545, USA

[3] Department of Hydrology and Water Resources, University of Arizona, Tucson, AZ 85721, USA

[4] Program in Applied Mathematics, University of Arizona, Tucson, AZ 85721, USA

[5] European Centre for Medium-Range Weather Forecasts, Reading, UK

[6] Géosciences, Université Montpellier - CNRS, Montpellier, 34095, France

[7] Dipartimento di Energia, Politecnico di Milano, Milan, 20133, Italy

1 Introduction

Recent developments in pore-scale modeling and imaging techniques are playing a key role in our understanding of the feedback between small-scale physics and macroscale modeling of flow and transport processes in natural and/or reconstructed porous media [18, 28]. In particular, high-resolution mapping and visualization of the structure of geologic materials allow detailed pore-scale modeling of flow in topologically complex pore spaces. Direct numerical simulation of flow through intricate microscopic structures yields insights into the effects of pore space characteristics on both microscopic and macroscopic flow properties. Modeling these phenomena has applications that range from groundwater flow and transport [29], to geophysics, including, e.g., petroleum extraction [28] and carbon sequestration [4], to filter design [15]. The spatially variable resistance to flow offered by the solid phase of a porous medium induces nonuniform fluid velocity fields where the observed dynamics range from stagnation to chaotic separation of fluid particle trajectories [19]. The effects of these flows taking place at the microscale can be embedded into continuum scale models, which can then be used to support field-scaled decision-making in oil, gas, and groundwater reservoir management.

As opposed to a pore-network modeling approach [4, 5, 34, 47] or a particle-based Lagrangian methodology, e.g., lattice Boltzmann [6, 8, 9, 16, 23, 26, 30] and smoothed particle hydrodynamics [44, 45], in the Eulerian methodology for simulating flow in microscopic pore structures, a particular numerical scheme, such as finite difference [26], finite element [10], or finite volume [11, 49], is selected, and the governing equations of flow are discretized accordingly. This discrete approximation is then numerically integrated on a computational mesh representing the pore space in a direct numerical simulation of flow. Comparisons of direct simulations of single-phase flow with particle-based methods [11, 26] revealed minimal and essentially negligible differences between the results obtained with the methodologies tested, but a clear advantage of the Eulerian methods was observed with regard to the required computation time. Lagrangian methods are slow to converge to a steady-state solution (for cases when the system evolves to attain steady-state) even when the codes are highly parallelized [9, 16].

Here, we compare three methodologies for the direct numerical simulation of gravity-driven, fully saturated, single-phase flow at the pore microstructure scale in two millimeter-scale natural rock samples. All three models are comparable in terms of resolution, but they are fundamentally dissimilar in terms of numerical methodologies and algorithmic complexity. We consider (a) the ANSYS® FLUENT® software [2], which integrates the Navier–Stokes equations using a finite-volume method on a hexagonal mesh; (b) the EULAG system [33], which uses conservative finite differences coupled with the volume-penalizing immersed boundary (IB) methodology to resolve the Navier–Stokes equations on a uniform Cartesian grid; and (c) the SSTOKES software, which uses standard second-order finite differencing and the ghost-cell IB method proposed by [35] to resolve the Stokes equations on meshes composed of cubic voxels. The natural porous media samples we consider consist of a quasi-pure silica sandstone and an oolithic limestone, which are characterized by distinctly different pore-scale structures. These types of geo-materials are found in several hydrogeology and petroleum engineering applications, and are viewed as typical media for the oil and gas industry. A detailed reconstruction of the pore space geometry of these systems was performed using X-ray microtomography [14], which provides information about the internal structure of natural samples in a nondestructive way [48].

Quantification of similarities/differences is performed according to (i) integral quantities, such as the Darcy flux, as well as (ii) the structure of the velocity distributions, characterized through their empirical probability density function (PDF) and the associated key statistical moments, including local correlations between velocity fields. These measurements are employed to probe in a statistical sense the internal similarities/differences across sample populations of velocities obtained for the two porous media analyzed using the three different computational systems. While the adopted methodologies are notably contrasting in terms of numerical schemes, our results show that they all produce results that are reasonably close to one another. In the case of the limestone sample, the structures of the velocity fields obtained using ANSYS FLUENT and EULAG are more alike than either with that obtained using SSTOKES. In the case of the sandstone sample, the structures of the velocity fields obtained by EULAG and SSTOKES are more like one another than either to the solution obtained using ANSYS FLUENT. So far as macroscopic quantities are concerned, ANSYS FLUENT and SSTOKES provide similar results in terms of the average vertical velocity for both of the complex microscale geometries considered, while EULAG tends to render larger velocity values with greater variability. The documented correspondence among the results supports the reliability of computational approaches to detailed pore-scale simulations.

The remainder of the paper is divided into three main sections. Section 2 describes the two natural rock samples

and the three modeling approaches in terms of geometrical description, mathematical formulation, and numerical techniques. Section 3 is devoted to the comparison of the results from the three different methodologies in terms of local and integral quantities. Concluding remarks are presented in Section 4.

2 Methods

2.1 Description of rock samples

We study flow through samples of two different (natural) rocks: (a) an oolithic limestone from the Mondeville formation of the middle Jurassic age, and (b) a Fontainebleau sandstone, both from the Paris Basin (France). The over-all dimensions of the analyzed blocks are $0.65 \times 0.65 \times 1.3$ mm^3 , and we refer to them as the limestone sample and the sandstone sample. The limestone is composed of millimeter-scale recrystallized ooliths, partially cemented with micritic calcite [13]. The limestone sample was sub-ject to carbonate dissolution performed under laboratory conditions that increased the total connected porosity of the sample from about $\phi_L \approx 6.8$ % to $\phi_L = 31.41$ %. The sandstone is a quasi-pure silica sandstone that is often used as a standard analog for sandstone reservoirs. Porosi-ties of samples of these sandstones usually range from 5 to 30 %, and grain sizes are relatively homogeneous, typically around 250 μm [7]. The sandstone sample is characterized by a total connected porosity $\phi_S = 7.05$ %. The porosity values provided here represent the connected pore network, i.e., the void space that connects the flow inlet and outlet boundaries.

The three-dimensional structure of each sample is reconstructed via synchrotron X-ray microtomography, with a voxel size of $\Delta z = 5.06$ μm [14]. Both samples were imaged using the ID19 beam at the European Synchrotron Radiation Facility (Grenoble, France). Figure 1a illustrates the structure of the pore space of the limestone sample by means of a set of horizontal cross-sections; Fig. 1b shows the vertical profile of surface porosity (each value is associ-ated with a volume of size 0.65 mm $\times$ 0.65 mm $\times$ Δz); and Fig. 1c depicts the sample probability density functions of pore sizes, S, normalized by the grid step, evaluated along the three Cartesian axes, x, y, and z and computed on the whole domain according to the methodology employed in [37]. Figure 2 depicts graphically the corresponding set of information for the sandstone rock.

Surface porosities computed along horizontal planes range between 13 and 50 % for the limestone and between 1.4 and 23 % for the sandstone. Each sample exhibits an abrupt change in porosity starting a little further than midway down the sample column and ending well before the bottom, the limestone showing an anomalous region of low porosity and the sandstone showing an anomalously high-porosity region. The empirical probability density functions (PDFs) of pore sizes (Figs. 1c and 2c) reveal that each system is relatively isotropic. When plotted on a semi-logarithmic scale, the PDF tails display a clear exponential decay for an intermediate range of pore size values, analo-gously to what observed by [37] for synthetically generated pore structures. The range covered by the pore size values in the limestone (i.e., the medium with largest porosity) is wider than in the sandstone in all directions.

2.2 Mathematical formulation of the flow problem

The governing equations for a single-phase, incompressible Newtonian fluid, i.e., water, fully saturating the pore space, are the transient Navier–Stokes equations,

$$\nabla \cdot \mathbf{v} = 0 \tag{1}$$

$$\frac{\partial \mathbf{v}}{\partial t} + \mathbf{v} \cdot \nabla \mathbf{v} = -\frac{1}{\rho} \nabla p' + \mathbf{g} + \nu \Delta \mathbf{v} \tag{2}$$

Here, Eqs. 1 and 2 respectively represent the mass and momentum conservation; $\mathbf{v}$ is the Eulerian fluid velocity vector, ν is the fluid kinematic viscosity, ρ is the fluid density, $p' = (p - p_0)$ is the relative pressure, and $\mathbf{g} = (0, 0, -g)$ is the gravity force (p, g, and p_0 respectively being pressure, gravity, and a constant reference pressure). Fluid density and kinematic viscosity are set respectively as $\rho = 1025$ kg m^{-3} and $\nu = 1 \times 10^{-6}$m^{2}s^{-1} for all simulations. No-slip boundary conditions, i.e., $\mathbf{v} = 0$, are enforced along pore walls boundaries.

The Reynolds number associated with flow through natural fractured and porous media is usually small enough to consider creeping-flow regime as a valid assumption [4, 11]. Under this assumption, the nonlinear term in Eq. 2 can be disregarded, and the governing equations are the incompressible Stokes equations, i.e.,

$$\frac{\partial \mathbf{v}}{\partial t} = -\frac{1}{\rho} \nabla p' + \mathbf{g} + \nu \Delta \mathbf{v} \tag{3}$$

together with Eq. 1 in the void space of the samples.

2.3 Problem setting

Comparisons among the ANSYS FLUENT, EULAG, and SSTOKES computational models are performed at steady-state flow conditions for both rock samples considered. We define steady-state conditions to be reached when the following criteria are met. First, the relative difference between the average velocity magnitude observed at two consecutive

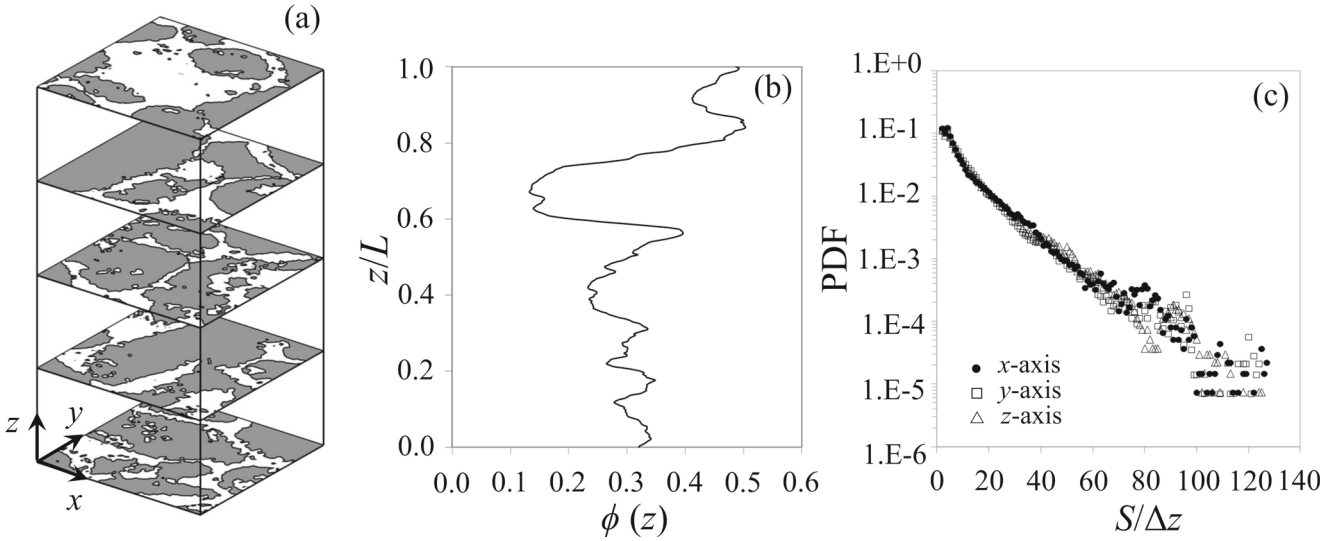

Fig. 1 Mondeville limestone: **a** Horizontal cross-sections, white regions represent the pore space; **b** vertical distribution of surface porosity; **c** empirical probability density functions (PDFs) of pore sizes, S, normalized by the grid step, $\Delta z = 5.06\ \mu$m, evaluated along the three Cartesian axes, x, y, and z, and computed on the whole domain

time steps, symbolized as t and $(t+1)$, is such that

$$\left| \frac{\langle |\mathbf{v}| \rangle_{t+1} - \langle |\mathbf{v}| \rangle_t}{\langle |\mathbf{v}| \rangle_t} \right| < 10^{-6} \tag{4}$$

$\langle \cdot \rangle$ being the sample average evaluated over all pore voxels. Second, the difference between the vertical (i.e., along direction z) component of velocity, w, observed at two consecutive time steps at corresponding nodal locations is such that

$$\frac{\langle |w(x, y, z, t+1) - w(x, y, z, t)| \rangle}{\langle |w(x, y, z, t)| \rangle} < 10^{-6} \tag{5}$$

ANSYS FLUENT and EULAG solve (1) and (2), while SSTOKES solves (1) and (3). All flow simulations are per-formed in the discretized domains of size 128 × 128 × 256 voxels depicted in Figs. 1a and 2a. Impermeable boundary conditions are set on the lateral sides of the samples for all of the approaches. In each case flow is gravity driven (i.e.,

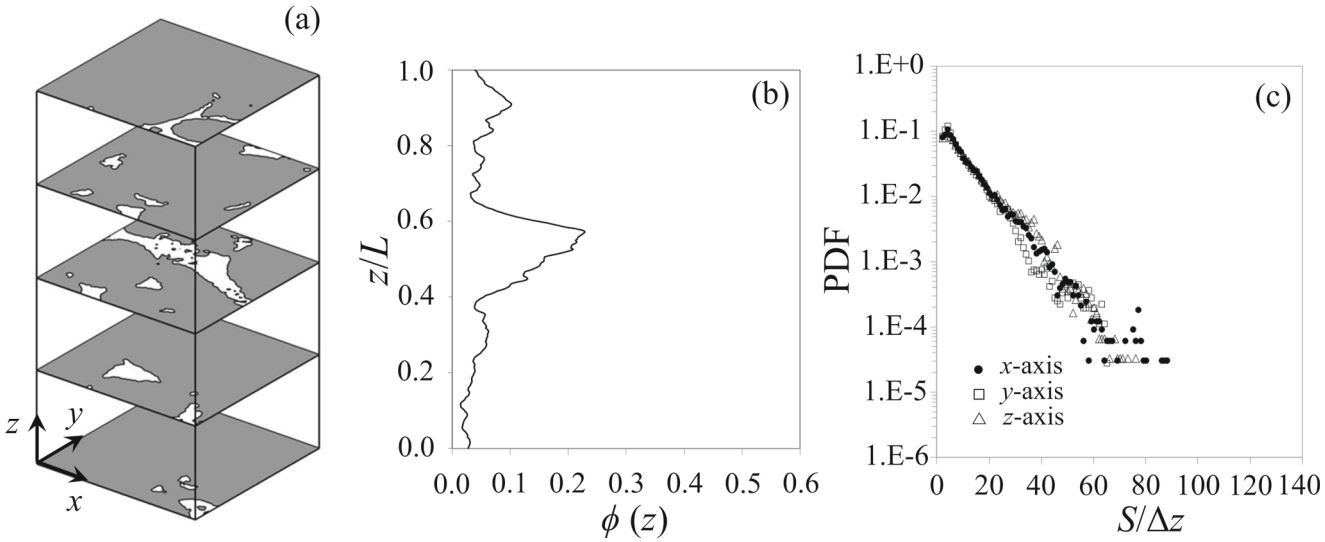

Fig. 2 Fontainebleau sandstone: **a** Horizontal cross-sections, white regions represent the pore space; **b** vertical distribution of surface porosity; **c** empirical probability density functions (PDFs) of pore sizes, S, normalized by the grid step, $\Delta z = 5.06\ \mu$m, evaluated along the three Cartesian axes, x, y, and z, and computed on the whole domain

Table 1 Mean, standard deviation (SD), and coefficient of variation (CV) of vertical velocity summed over all points in the pore space of the Mondeville limestone sample

	Mean ($\times 10^{-4}$m s^{-1})	SD ($\times 10^{-4}$ m s^{-1})	CV
EULAG	−3.23	4.55	1.41
SSTOKES	−1.93	2.76	1.43
ANSYS FLUENT	−1.93	3.00	1.55

induced by **g**) and takes place predominantly in the vertical direction, z. Periodic boundary conditions are employed in EULAG, $\mathbf{v}(x, y, 0) = \mathbf{v}(x, y, L)$, along the vertical direction, together with the corresponding periodic boundary conditions for the gradient of relative pressure in Eq. 1. Benefits of considering periodic boundaries include the ability to handle blocked flows in incompressible fluid settings and to ensure compatibility of initial conditions with the governing equations. It has to be noted that ensuring flow periodicity requires the (physical) domain to be periodic. With synthetically generated virtual media, system periodicity can be achieved during the generation process [20]. Periodicity for a real rock sample is achieved by mirroring the (generally nonperiodic) sample image along the vertical direction. The resulting medium is then symmetric with respect to the middle horizontal plane. The same geometric model and periodic conditions are adopted for consistency within the ANSYS FLUENT and the SSTOKES software environments. As a result of this vertical mirroring, the size of each simulated system is $128 \times 128 \times 512$ voxels. Only the results associated with the original sample with size $128 \times 128 \times 256$ voxels are analyzed and presented in Section 3.

2.4 Numerical methods

Major challenges for the direct simulation of flow in explicit pore structures include (a) the representation of the complicated geometry of the porous microstructure and (b) the enforcement of no-slip boundary conditions along pore walls. Accurate representation of a pore space at the scale and resolution of interest associated with a binary digital image of pore spaces can be achieved using smooth, unstructured meshes and refined octree grids that conform to the geometry of the pore space [21, 49]. These variable resolution meshes can be refined along pore walls to resolve boundary layer effects in the flow field that occur at length scales smaller than the resolution of the imaged pore spaces. Generating conformal meshes to represent the intricate geometries that make up real porous microstructures is demanding, both in terms of computer memory and computational time. A first-order accurate stair-step representation of the void space, where the pore space is discretized by structured hexahedral cells or cubic voxels, offers a meshing approach that partially overcomes these demands. Although the accuracy of the representation of the solid boundary is somewhat compromised, stair-stepping yields meshes that are efficient and low cost but accurate within bounds of computational error for simulations of flow through pore microstructures [18]. Gerbaux et al. [11] compared the performance of tetrahedral and hexagonal meshes, and concluded that the latter required less computational resources, with minimal discrepancies between the flow results. Analogous results stem from pore-scale flow simulations of Peszynska and Trykozko [32], who tested unstructured hexahedral and body-fitted mesh performances within the ANSYS FLUENT software environment.

Once the mesh has been selected, no-slip boundary conditions can be directly enforced by spatially varying the difference stencil to conform with the pore space geometry. The efficient implementation of this approach still remains a critical challenge. A promising alternative is given by the immersed boundary method (IB) [27]. According to the latter, no-slip boundary conditions are enforced at the fluid-solid interface by inserting a fictitious forcing term into the governing equations of flow to mimic the resistance offered by the solid wall boundaries. The advantage of this approach is that a uniform Cartesian grid can be employed to simulate flow in complex pore spaces and the difference stencil is uniform throughout the computational domain. This uniformity makes the method well suited for existing and future HPC architectures, such as GPUs and MIC. The IB has been successfully applied to two- [24, 25] and three-dimensional

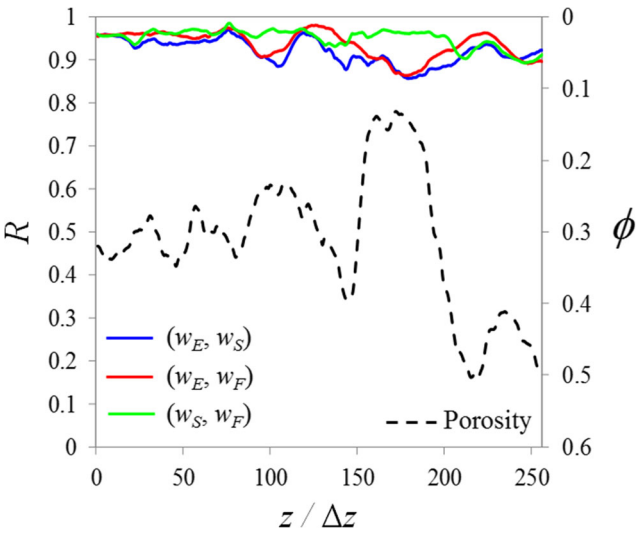

Fig. 3 Mondeville limestone. Cross-correlation coefficients R by vertical level of the cross-section (here, w_E, w_S, and w_F respectively denote vertical velocities computed by means of EULAG, SSTOKES, or ANSYS FLUENT). The vertical profile of porosity, ϕ, is also reported

Table 2 Mean and standard deviation (SD) computed for four selected cross-sections of the Mondeville limestone sample

LEVEL	Mean ($\times 10^{-4}$ m s^{-1})			SD ($\times 10^{-4}$ m s^{-1})		
	EULAG	SSTOKES	ANSYS FLUENT	EULAG	SSTOKES	ANSYS FLUENT
65	−3.35	−2.02	−2.02	3.56	2.26	2.42
120	−3.81	−2.30	−2.30	5.83	3.79	4.02
180	−6.88	−4.01	−3.99	7.95	4.48	5.05
215	−2.00	−1.20	−1.22	2.59	1.56	1.81

[17–19, 36, 37, 43] simulations of flow in microscopic pore structures.

Immersed boundary methods are naturally divided into continuous and discrete (or direct) forcing approaches, depending on the way the fictitious forcing term is implemented. In the continuous approach, the forcing term is included in the original continuous form of the governing equations, while in the discrete approach, the fictitious boundary force is introduced after the equations have been discretized. Examples of the continuous forcing class include volume penalizing [1] and feedback forcing methods [12] that set the additional forcing term to be proportional to the flow velocity. An example of the discrete-forcing class of IB approaches is the ghost-cell method [31, 46] where the computational (discretized) domain is partitioned into physical and ghost-cell sub-domains. The physical sub-domain contains only computational cells associated with the fluid, whereas computational cells that reside within the solid domain and have at least one neighboring cell in the fluid phase form the ghost-cell sub-domain. Velocity values are computed for each ghost cell through interpolation so that the desired boundary conditions at the fluid-solid interface are enforced on the basis of a "projection node" located within the fluid region.

2.5 Computational systems

ANSYS FLUENT The first computational system employed in this study is embedded in the ANSYS FLUENT software and uses a finite-volume method to numerically integrate (1) and (2) on a first-order hexagonal grid representation of the fluid domain. FLUENT is a commercial code maintained by ANSYS, Inc., (www.ansys.com). A segregated transient formulation using the non-iterative pressure implicit splitting of operators (PISO) algorithm [2, 22] for pressure-velocity coupling is employed. The advection term in Eq. 2 is discretized using a second-order upwind scheme developed for unstruc-tured meshes and limiting the gradient of the advected quantity to avoid occurrence of new maxima or minima [3]. Pressure is discretized using a body force weighted scheme and linear second-order accurate interpolations are used for the discretization of the viscous term [2]. All variables are collocated on the hexahedral mesh. The faces of the hexahedral elements lying at the fluid–solid interface define the boundary position and no-slip conditions are set directly at the face center using the adopted finite-volume method. The time step employed in the simulations performed with ANSYS FLUENT is $\Delta t = 2.5 \times 10^{-6}$ s. For this study, the

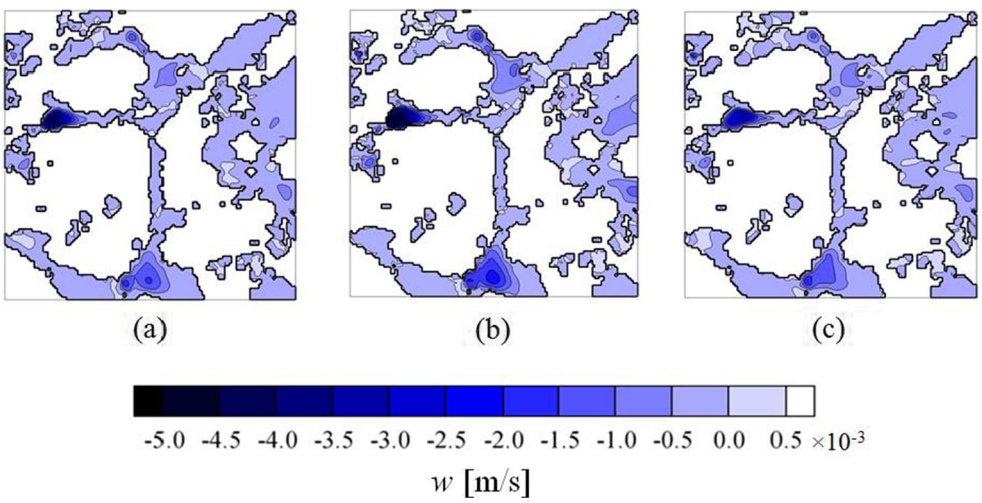

Fig. 4 Spatial distribution of the vertical velocity component, w, obtained by **a** ANSYS FLUENT, **b** EULAG, and **c** SSTOKES along the plane at elevation $z = 127\Delta z$ of Mondeville limestone

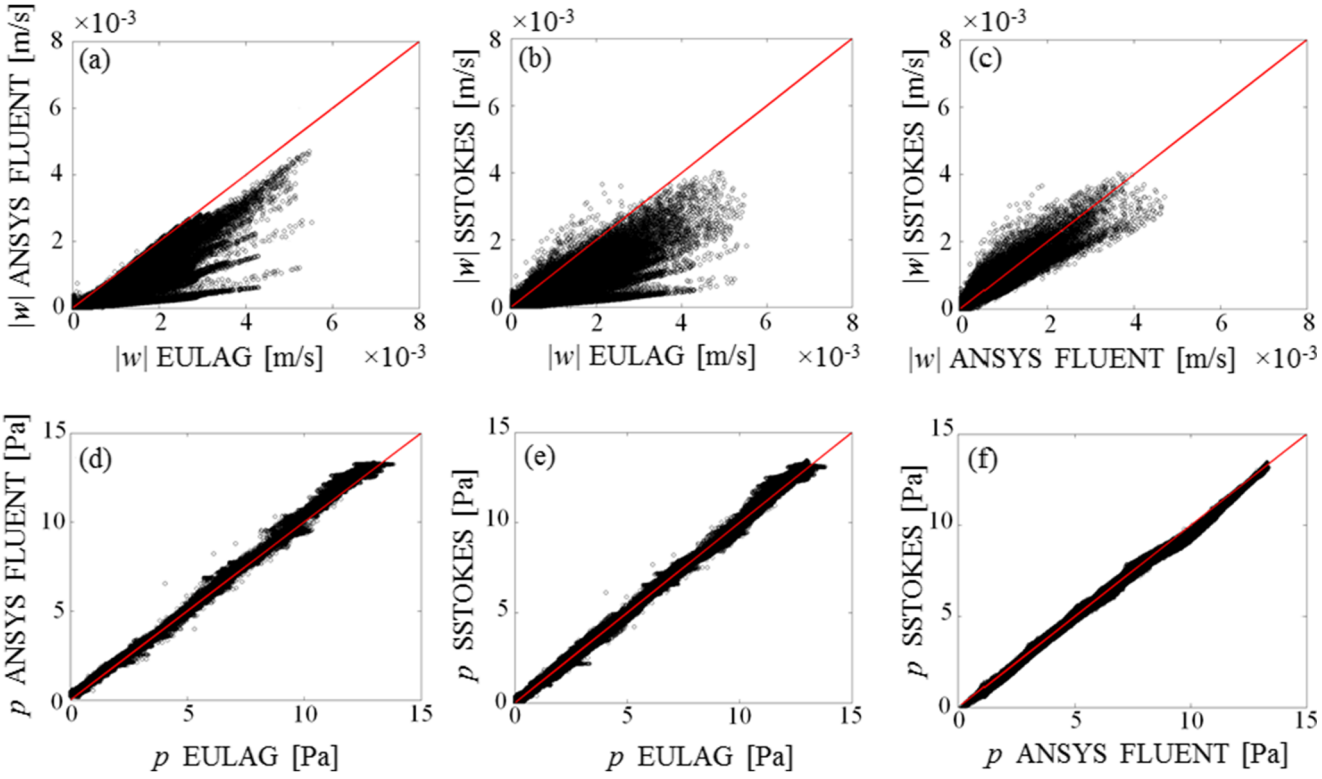

Fig. 5 Scatter diagrams of values of **a–c** $|w|$ and **d–f** p computed at the nodes within the fluid region by the three methodologies analyzed for Mondeville limestone

code was run in parallel on 12 CPUs, on a Dell™ PowerEdge™ R410 machine, with 2x Intel® Xeon® X5670 (6 cores at 2.93 GHz and 32 GB of RAM).

EULAG The second system we use in this study is the modification of the EULAG system provided by Smolarkiewicz and Winter [43]. EULAG is an open source code and can be obtained by contacting the developers at http://www2.mmm.ucar.edu/eulag/. In this framework, no-slip boundary conditions are enforced using a continuous forcing IB method. Formally, a modification of the momentum (2) allows for the implicit enforcement of no-slip conditions along the fluid-solid interface,

$$\frac{\partial \mathbf{v}}{\partial t} + \mathbf{v} \cdot \nabla \mathbf{v} = -\nabla \pi' + \mathbf{g}\frac{\rho'}{\rho} + \nu \Delta \mathbf{v} - \alpha \mathbf{v} \tag{6}$$

As in Eq. 2, here, primes refer to perturbations with respect to static ambient atmospheric conditions charac-terized by a constant density, ρ_0, and pressure, p_0, i.e., $\pi' = (p - p_0)/\rho$ and $\rho' = \rho - \rho_0$, where $\rho =$ const $>> \rho_0$ denotes the density of water. The fictitious repelling body force, $\alpha \mathbf{v}$, is inserted in the right side of

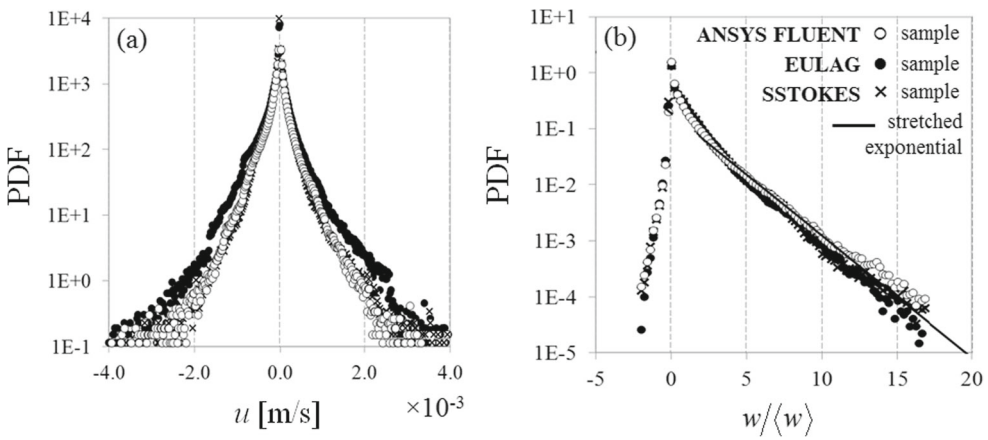

Fig. 6 Empirical PDF of **a** u and **b** $w/\langle w \rangle$—where $\langle \cdot \rangle$ represents the sample average—computed over the whole fluid domain with the three methodologies analyzed for Mondeville limestone

Table 3 Comparison of mean Darcy flux computed using the three methodologies analyzed

	Mondeville Limestone	Fontainebleau Sandstone
Model	q_{ave} ($\times 10^{-5}$ m s^{-1})	q_{ave} ($\times 10^{-6}$ m s^{-1})
EULAG	−9.97	−2.16
SSTOKES	−6.06	−1.04
ANSYS FLUENT	−6.08	−1.13

Table 4 Mean, standard deviation (SD), and coefficient of variation (CV) of vertical velocity summed over all points in the pore space of the Fontainebleau sandstone sample

	Mean ($\times 10^{-5}$ m s^{-1})	SD ($\times 10^{-5}$ m s^{-1})	CV
EULAG	−3.07	7.90	2.57
SSTOKES	−1.48	4.45	3.01
ANSYS FLUENT	−1.60	3.81	2.38

the momentum (2) to circumvent the difficulty of gener-ating a conforming mesh representation of the void space. In Eq. 6, $\alpha(\mathbf{x})$ vanishes when vector location $\mathbf{x}$ is in the pore volume and is large otherwise. Intuitively, setting $\alpha(\mathbf{x}) = 0$ within the pore volume admits Navier–Stokes flows away from the solid boundaries and (6) reduces to Eq. 2; on the other hand, requiring $\alpha(\mathbf{x}) \to \infty$ within the solid prevents flow therein [41, 43]. The governing sys-tem of Eqs. 1 and 6 is cast in the conservation form and integrated numerically at every computational node in the uniform Cartesian grid using a second-order-accurate, semi-implicit, non-oscillatory forward-in-time (NFT) approach. Theoretical bases, implementation, and applications of the approach are broadly documented [38–40, 42]. The NFT approach is a flux-form finite difference method, an equiva-lent of finite-volume approach on a Cartesian grid. The res-olution is globally semi-implicit: convective and diffusive terms are solved explicitly, whereas all the forcing terms in Eq. 6 are dealt with implicitly using a preconditioned Krylov method to solve the resulting elliptic equation. Details of the discretized set of equations and of the numer-ical integration procedure are found in [43]. The EULAG code is run in parallel using 8 CPUs on the Dell™ Pow-erEdge™ R410 machine with 2x Intel® Xeon® X5670 (6 cores at 2.93 GHz and 32 GB of RAM) for the lime-stone sample and using 16 CPUs on the Dell™ Pow-erEdge™ R620 machine with 2x Intel® Xeon® E5-2680 (8 cores at 2.70 GHz and 64 GB of RAM) for the sand-stone. For our simulations, we follow Smolarkiewicz et al. [43] and set $\alpha^{-1} = \Delta t/2 = 2 \times 10^{-8}$s. This value is con-siderably smaller than the time scales associated with the effects of viscous and gravity forces evaluated at the grid scale that are respectively $(\Delta z)^2/\nu = 2.5 \times 10^{-5}$s and $(2\Delta z/g)^{1/2} = 1 \times 10^{-3}$s.

SSTOKES The third system we use is the SSTOKES code [35], which can be made available upon request. SSTOKES enforces internal boundary conditions using a discrete IB method, and the space and time derivatives of Eqs. 1 and 3 are discretized using second-order centered-difference and forward-difference schemes, respectively, and solved implicitly. SSTOKES uses a staggered approach where pressure is defined at the cell center, and velocity components are considered along the cell faces. In this framework, velocities tangential to the solid boundary are not defined at the boundary itself. The ghost-cell IB method is used to enforce the no-slip boundary conditions along internal solid boundaries. At each time step, flow variables in the ghost cells outside of the void space are determined using linear interpolation with the neighboring image points inside of the void space to enforce no-slip conditions exactly along the void–solid interface. The computational mesh is a first-order cubic stair-step approximation of the void space embedded within the solid phase. The computational parameters considered for the SSTOKES system are those controlling the convergence to a steady-state solution. The time step employed in the simulations performed with SSTOKES is $\Delta t = 2 \times 10^{-8}$s. The SSTOKES code is not parallelized. In this study, it was run on one core of the HP Z800 workstation equipped with 2x Intel® Xeon® E5-2680 (8 cores at 2.7 GHz and 64 GB RAM).

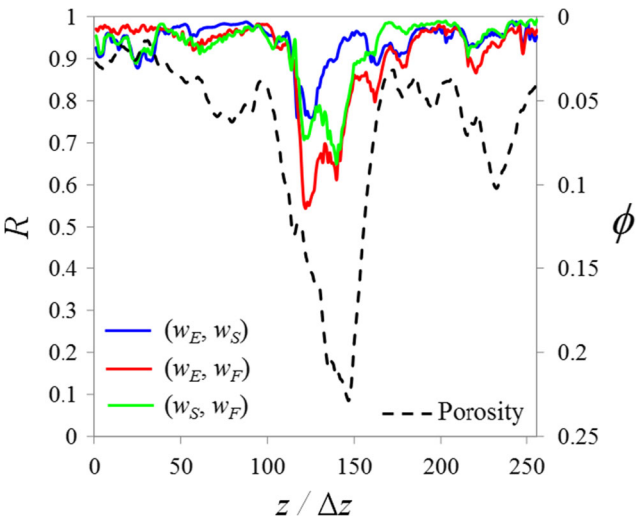

Fig. 7 Fontainebleau sandstone. Cross-correlation coefficients R by vertical level of the cross-section (here, w_E, w_S, and w_F respectively denote vertical velocities computed by means of EULAG, SSTOKES, or ANSYS FLUENT). The vertical profile of porosity, ϕ, is also reported

Table 5 Mean and standard deviation (SD) of vertical velocity computed on four selected cross-sections of the Fontainebleau sandstone sample

LEVEL	Mean ($\times 10^{-5}$ m s^{-1})			SD ($\times 10^{-5}$ m s^{-1})		
	EULAG	SSTOKES	ANSYS FLUENT	EULAG	SSTOKES	ANSYS FLUENT
50	−0.57	−0.28	−0.25	0.46	0.27	0.19
100	−0.46	−0.23	−0.24	1.44	0.81	0.71
140	−0.11	−0.05	−0.07	0.19	0.11	0.11
200	−0.52	−0.26	−0.26	1.68	0.99	0.84

2.6 Metrics for system comparison

The analysis of the simulation results compares the capabilities of the three considered methodologies to simulate pore-scale flow fields in natural porous media at the millimeter scale. The local Eulerian vertical velocity component, w, is a key quantity of interest in the comparison due to its relevance in transport processes occurring at the scale of porous microstructure. The comparison of the steady-state flow fields is performed in terms of the structure of the velocity and pressure fields, the distribution of the vertical velocities, as well as integral quantities, namely the Darcy flux, $q(z)$ computed at steady-state, i.e.,

$$q(z) = \frac{1}{N} \sum_{i=1}^{N_P(z)} w_i \tag{7}$$

In Eq. 7, $N_P(z)$ is the number of nodes in the pore space of the horizontal plane at elevation z; $N = 16,384$ is the total number of nodes at a given horizontal cross-section; w_i is the vertical component of the Eulerian velocity calculated at node i. Since nowadays we still do not have at our disposal high-quality laboratory flow experimental data which can be employed for a point-by-point comparison against computed values in real rock samples of the size we consider, the structures of the resulting velocity fields are also compared in terms of their empirical probability density functions (PDFs) and associated main statistics. These include the coefficient of variation related to the calculated local velocities as well as the point-wise cross-correlation coefficient between vertical velocity fields at every horizontal cross-section of the system, defined as

$$R_{ij} = \frac{\left\langle \left(w_i - \langle w_i \rangle\right)\left(w_j - \langle w_j \rangle\right)\right\rangle}{\sigma_{w_i}\sigma_{w_j}} \tag{8}$$

where $i, j = E, S$, or F (E, S, or F respectively denoting EULAG, SSTOKES, or FLUENT), and $\langle w_i \rangle$ and σ_{w_i} respectively are average and standard deviation of nodal values of w_i computed across a given cross-section located at vertical elevation z.

When considered jointly with integral quantities, these metrics provide additional layers of information regarding the structure of the velocity fields and allow investigating in a statistical sense the similarities/differences between the distributions of velocity. The standard deviation provides information about the variability of the spatial distribution of the values of a given quantity, and the coefficient of variation is an indicator of the intrinsic variability resulting from each computational system after accounting for the multiplicative effect of the mean. The cross-correlation

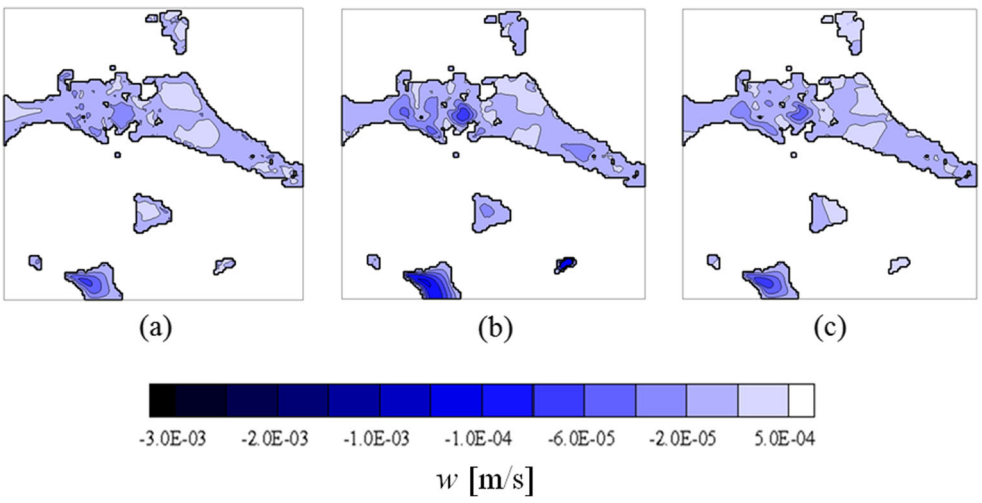

Fig. 8 Spatial distribution of the vertical velocity component, w, obtained by **a** ANSYS FLUENT, **b** EULAG, and **c** SSTOKES along the plane at elevation $z = 127\ \Delta z$ of Fontainebleau sandstone

coefficient is a measure of the linear dependence between two variables and quantifies (in a statistical sense) the degree of similarity of the flow solutions obtained by two computational suites. A qualitative description and comparison of the contour plots of velocities of the cross-sections is also provided. Flow statistics such as mean vertical velocity, standard deviation, and cross-correlation are calculated over the total number of nodes in the pore space, i.e., $N_P(z)$ within a cross-section, or $N_{P,TOT}$ for the entire volume.

3 Results

3.1 Mondeville limestone sample

The three computational systems produce fluid velocities that are the same order of magnitude, i.e., $O(10^{-4}$ m s$^{-1})$. The Reynolds number $Re = UL/\nu$, L and U respectively being the mean hydraulic radius and mean vertical velocity, is of order $O(10^{-3})$ for all approaches.

It can be noted that EULAG produces higher average vertical velocities (by a factor of about 5/3) with more spatial variability than either SSTOKES or ANSYS FLUENT (Table 1). The mean values associated with SSTOKES and ANSYS FLUENT are essentially the same, and ANSYS FLUENT shows slightly enhanced overall variability with respect to SSTOKES. Values of the coefficient of variation (CV) obtained through all three systems are about the same, with ANSYS FLUENT yielding a slightly higher value than the other two.

Linear correlations between horizontal cross-sections of vertical velocity fields produced by the simulation systems are high (> 0.85) at all elevations within the limestone sample (Fig. 3), indicating a general agreement among the structures of the fields. This is consistent with the values of CV listed in Table 1. Nonetheless, the two-sample Kolmogorov–Smirnov test rejects the hypothesis that the simulated vertical velocities within a cross-section are from the same distribution at the 5 % significance level. Correlations between EULAG and the other two systems are somewhat reduced at elevations ($\approx 150 - 200\ \Delta z$) where a large decrease in local porosity is observed.

Cross-sectional means and standard deviations of vertical velocities are consistent with the observed pattern resulting in higher velocity and variability for EULAG simulations than for the other two systems (Table 2). The results listed in Table 2 are associated with cross-sections which are all $l \approx 30\ \Delta z$ apart. The mean values associated with ANSYS FLUENT and SSTOKES results coincide, and ANSYS FLUENT simulations exhibit somewhat higher standard deviations than SSTOKES does. All three computational systems produce relatively higher (more negative) vertical velocities in the region of low porosity (e.g., at an elevation of about 180 Δz) than at other elevations, and all three show relatively lower (less negative) velocities at elevations (e.g., 215 Δz) where porosity is highest. Similar results (not reported) are obtained on other sets of cross-sections, extracted using the same criteria. Variability, as measured by standard deviation, follows the same pattern of relatively high variability where porosity is lowest (e.g., 180 Δz) and resistance to flow is highest, and low variability where porosity is highest and resistance to flow is least.

Contour plots of the vertical velocity component produced by each model in the plane at elevation $z = 127\Delta z$ produce similar patterns for the flow field, with EULAG exhibiting higher overall fluxes and more spatial variability in the velocity values than either SSTOKES or ANSYS FLUENT (Fig. 4). In each case, the majority of the velocity field is stagnant, or nearly so. This is consistent with the results of [17] who found that most of the flux through a sample of realizations of synthetically generated porous media occurs in a relatively small percentage of the pore volume. Regions of higher velocity in the upper left quadrant and lower middle part, indicated by dark color in Fig. 4, are more finely resolved by ANSYS FLUENT and EULAG than SSTOKES. The sharp gradients that form in the velocity field due to the variable resistance offered by the pore wall geometry are not as apparent in the solution provided by SSTOKES. Qualitatively similar results are obtained for other planes (not shown).

Scatter plots of values of $|w|$ computed at all nodes within the fluid region by the three methodologies are depicted in Fig. 5a–c. These plots illustrate the general agreement between the ANSYS FLUENT and SSTOKES estimates (values of $|w|$ distributed around the unit slope line) with EULAG estimates that are relatively higher than either (results that consistently lie below this line). Complementary scatter plots of nodal values of fluid pressure are depicted in Fig. 5d–f. These fall on the unit slope line indicating that the three methodologies produce consistently similar results for pressure.

Empirical PDFs of horizontal velocities (u) and normalized vertical velocities ($w/\langle w\rangle$, $\langle\cdot\rangle$ representing sample average) are depicted in Fig. 6a–b. Both PDFs are based on estimates from the whole fluid domain. The horizontal velocity component along the y direction, v, displays similar behavior to u (not shown). Horizontal velocity components from all three simulations display symmetric distributions centered on zero. However, the PDF based on EULAG is characterized by higher tails, indicating a tendency to assign more probability to the tails of the distribution. The normalized vertical velocity component

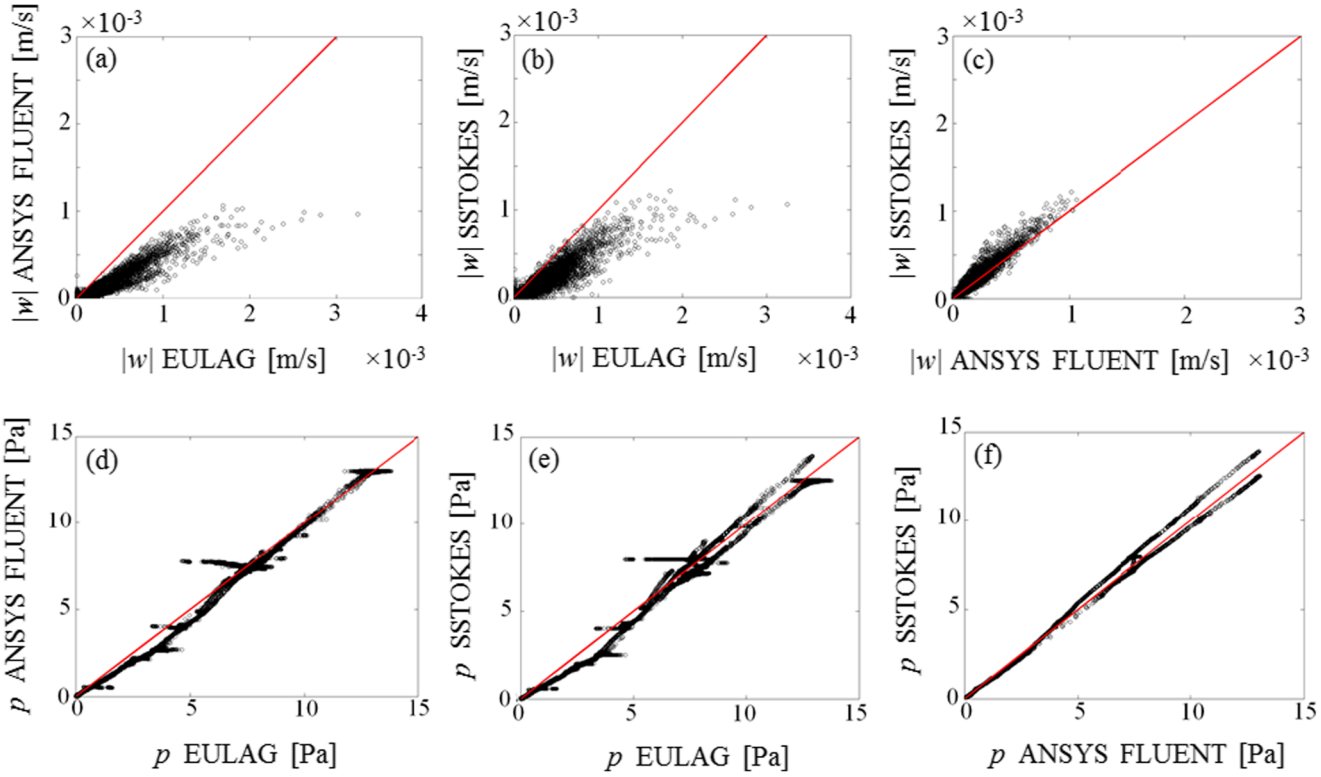

Fig. 9 Scatter diagrams of values of **a–c** $|w|$ and **d–f** p, computed at the nodes within the fluid region by the three methodologies analyzed for Fontainebleau sandstone

$w/\langle w\rangle$ exhibits clear positive skewness in all three examples, consistent with the gravity-driven flow regime studied. Following [37], a stretched exponential model is juxtaposed to the data in Fig. 6b: the decay of the tails of all three PDFs is consistent with this model, which includes the exponential trend (i.e., linear trend in semi-log scale) as a particular case. The occurrence of only a small fraction of nodes associated with an upward value of w (i.e., negative tail of the PDF) indicates that there is only a limited set of localized recirculation paths in the internal structure of the pore space.

When normalized by the sample average, the tail of the PDF obtained using ANSYS FLUENT is slightly higher than that obtained via EULAG or SSTOKES, which is consistent with the CV values listed in Table 1.

The three methods yield values for the (macroscopic) mean Darcy flux, q_{ave}, [Eq. 7, averaged over all horizontal cross-sections] that are of the same order of magnitude (Table 3). Consistent with the results illustrated in Fig. 5, the estimation of q_{ave} provided by EULAG is larger than those provided by SSTOKES or ANSYS FLUENT.

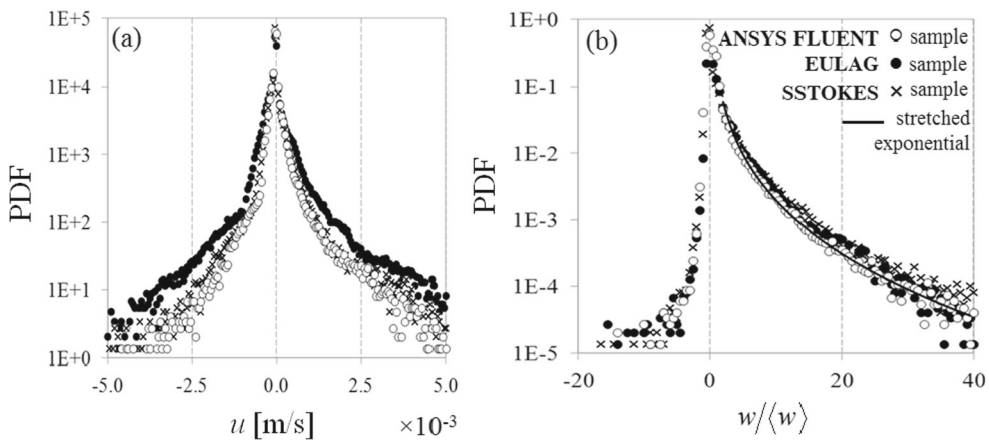

Fig. 10 Empirical PDF of **a** u and **b** $w/\langle w\rangle$—where $\langle\cdot\rangle$ represents the sample average—computed over the whole fluid domain with the three methodologies analyzed for Fontainebleau sandstone

3.2 Fontainebleau sandstone sample

In general, results of comparisons among simulated states are similar to those observed for the limestone. As in the case of the limestone medium, the three systems produce fluid velocities that are of the same order of magnitude, in this case O(10^{-5} m s^{-1}), and Reynolds number, which is of order O(10^{-4}). EULAG renders higher average vertical velocities (now by a factor of about 2) with more spa-tial variability than either SSTOKES or ANSYS FLUENT, as shown by the results listed in Table 4. The mean val-ues rendered by SSTOKES and ANSYS FLUENT are also essentially coinciding, with SSTOKES showing slightly more pronounced overall variability than ANSYS FLUENT. The CVs produced by all three systems are very similar also in this case, with SSTOKES yielding a slightly higher value than the ANSYS FLUENT or EULAG for this sample. Simulation results of vertical velocity in the sandstone medium are intrinsically more variable than those observed in the more porous limestone.

Linear correlations between horizontal cross-sections of vertical velocity fields produced by the simulation systems are high (> 0.85) at all elevations, except over the set of elevations ($\sim 120 - 180\ \Delta z$) where porosity increases abruptly (Fig. 7). Correlations between all three pairs of the simulations are considerably reduced there, with the EULAG–SSTOKES pair being least affected. Similar to what is noticed for the limestone rock sample, the two-sample Kolmogorov–Smirnov test rejects the hypoth-esis that the simulated vertical velocities within any given cross-section are from the same distribution at the 5 %significance level.

Cross-sectional means and standard deviations of vertical velocities are in line with the general pattern of higher velocity and variability in EULAG simulations (Table 5). The means of ANSYS FLUENT and SSTOKES estimates are again practically the same, but this time it is the SSTOKES simulations that exhibit somewhat higher standard deviations than ANSYS FLUENT. All three systems produce relatively lower (less negative) vertical velocities in the region of high porosity (e.g., at elevation $z = 140\ \Delta z$) than at other elevations. Similar results (not reported) are obtained on other sets of cross-sections extracted using the same criteria as above. Variability, as measured by standard deviation, follows the same pattern of relatively high variation where porosity is lowest and resistance to flow is highest and low variability where porosity is highest and resistance to flow is least.

Contour plots of simulated vertical velocities in the plane at the middle elevation $z = 127\ \Delta z$ produce roughly similar patterns for the flow field (Fig. 8). The majority of the velocity field is stagnant, or nearly so, with highest flows occurring in the middle of the large pore spanning the cross-section and in the isolated pore toward the bottom, consistent with the observation of [17] that flow in pore spaces tends to occur in a relatively small percentage of the pore volume. EULAG exhibits higher flow overall and more variability than either SSTOKES or ANSYS FLUENT.

Scatter plots of values of $|w|$ computed at all nodes within the fluid region by the three methodologies are depicted in Fig. 9a–c. As in the case of the limestone sample, these illustrate the general agreement between the ANSYS FLUENT and SSTOKES estimates, EULAG estimates being relatively higher than either. Scatter plots of nodal values of fluid pressure are depicted in Fig. 9d–f. These are close to the line of unit slope indicating again that the three methodologies produce consistently similar results for pressure.

Empirical PDFs (Fig. 10a–b) of horizontal, u, and normalized vertical, $w/\langle w\rangle$, velocities are based on estimates from the whole fluid domain, which is consistent with the analysis of the limestone sample. The PDF for u is symmetric and centered on zero, and EULAG distributes more probability to the tails of the distribution than either SSTOKES or ANSYS FLUENT. The normalized vertical velocity component is again skewed in the direction of flow. Figure 10b highlights that, similar to what observed for the limestone, the positive tails of the normalized velocity component decay following a stretched exponential model [37]. In this case, the tail of the PDF obtained using ANSYS FLUENT is slightly lower than that associated with the other two samples.

The value of the mean Darcy flux q_{ave} provided by EULAG exceeds those resulting from SSTOKES and ANSYS FLUENT by a factor of about two (see Table 3).

4 Summary and conclusions

Direct numerical simulations of fully saturated, gravity-driven flow are performed in millimeter-scale digitally reconstructed images of a high-porosity (31 %) limestone sample and a low-porosity (7 %) sandstone sample using three different Eulerian approaches: (a) ANSYS FLUENT, (b) the EULAG system, and (c) the SSTOKES code. These computational systems vary widely in terms of their algorithmic complexity and differ in terms of the associated numerical methodologies, enforcement of no-slip boundary conditions on internal walls, parallelization, and implementation of the Poisson solver. The resulting steady-state flow solutions are compared in terms of global quantities, the empirical probability density function (PDF) and associated main statistical moments of the local velocity fields.

When performing comparisons of computational results obtained with diverse codes, the notion of accuracy is poorly defined without a benchmark against which the solutions

can be compared. Because nowadays we still do not have at our disposal high-quality and high-resolution laboratory flow experimental data against which a pointwise comparison of calculated quantities can be accomplished in real rock samples of the size we consider, and it is virtually impossible to state without ambiguities if one solution is more accurate than another one. However, the distributions of velocity can be probed to assess similarities and differences between the computational methods. To do so, we consider the local structure of the velocity field, empirical PDFs of vertical and horizontal components of velocity and pressure, the first two moments of the velocity distributions, as well as the cross-correlation coefficient between the vertical velocities rendered by the codes we analyze at level planes. Beyond first-order comparisons, such as the mean Darcy flux, the higher order moments and cross-correlations provide information about the structure and similarities of the velocities fields in a statistical sense.

Given that the methods are notably different in a num-ber of ways, it is remarkable that they produce results that are reasonably close to one another. Using the metrics mentioned above, it was observed that the simulation results are similar with respect to (i) the overall structure of the empirical PDF of horizontal and vertical velocity components (Figs. 6 and 10), (ii) the structure of the spatial distribu-tion of velocities as revealed by cross-correlations (Figs. 3 and 7) and pattern (Figs. 4 and 8), and (iii) the magnitude of macroscopic parameters, specifically mean Darcy flux (Table 3), although they differ in details. Notably, the Darcy fluxes computed by the three methodologies are all of the same order of magnitude for a given sample. We note that in principle one could estimate Darcy flux on a rock core of characteristic length of the order of 10^{-3} m. A straightforward calculation shows that in case of such a rock sample the relative measurement errors on permeability and flux would be of about 130 and 250 %, respectively. However, these estimates should only be considered as purely theoretical since setting up such measurements is highly difficult with currently available resources, due to (a) difficulties in the preparation of the sample and (b) the smallness of the pressure drop, which is notably complex to be mea-sured. On the basis of these considerations, we conclude that Darcy flux values obtained using the computational suites considered would be within theoretical bounds associated with what would be a hypothetical laboratory experiment on millimeter-scale samples.

The three simulation environments produce steady-state flow fields that differ in their local details. When considering the pore-scale quantities associated with the Mondeville limestone, the similarity between the solutions obtained using ANSYS FLUENT and EULAG suggests that steep gradients in the velocity field, which result from the wider pores and nonuniform resistance offered by the variable geometry of the pore space, are more finely resolved when the nonlinear term in the Navier–Stokes equations is retained (Figs. 3 and 4). In the case of the Fontainebleau sandstone, the structure of the velocity fields obtained using EULAG and SSTOKES agree more than either does with ANSYS FLUENT (Figs. 7 and 8). In this low-porosity sample, solutions obtained using EULAG and SSTOKES capture the spatial influence of the geometry and topology of the pore space on the velocity field.

When considering upscaling of flow solutions to macroscopic quantities, including Darcy flux and thus permeability, the most relevant difference among the methodologies is the relatively large flow velocities computed by EULAG compared to ANSYS FLUENT and SSTOKES (Figs. 5 and 9 and Table 3). We also note that if simulation of pore-scale flow is aimed at understanding the influence of pore space geometry and topology on local fluid dynamics, then EULAG appears to provide consistent results with respect to structure and variability of the velocity fields in these two samples. The computed Reynolds numbers, $O(10^{-3}/10^{-4})$, might not be completely consistent with the assumptions upon which the Stokes equation rests. The observed difference in Darcy flux between EULAG and FLUENT could also result from the adopted numerical scheme to resolve the advective term in the corresponding momentum equations. FLUENT uses an upwinding scheme, which are numerically diffusive, and could result in the underesti-mation of the flux due to numerical diffusion. Otherwise, EULAG uses a nonlinear flux-limiting advection scheme to resolve high gradients and minimize numerical diffusion, which is consistent with the highest value obtained for the Darcy flux. This notwithstanding, we remark that the computed values could still be considered as comprised within theoretical laboratory measurement error bounds, as discussed above.

When compared across the two media investigated here, the Darcy fluxes in the limestone (see Table 3) sample are larger than those computed for the sandstone, consistent with the significant difference between the porosities (31 to 7 %) of the two rock samples. The associated empirical PDFs of horizontal components, u, and normalized vertical components, $w/\langle w\rangle$, of velocity are qualitatively similar (Figs. 6 and 10). The positive skewness of the PDFs of $w/\langle w\rangle$ obtained from all three simulations (Figs. 6b and 10b) reflects the dominant downward direction (i.e., in the direction of the negative z-axis) of flow, consistent with the gravity-driven flow regime studied. In general, the three computational systems analyzed produce normalized vertical velocities exhibiting about the same level of variability. This similarity indicates that the intrinsic variability of the results among these computational systems arises primarily from a multiplicative effect that is cancelled through normalization by the means. The small fraction of nodes

associated with a positive value of w (the negative tail of the PDF) suggests that there is only a limited set of localized recirculation paths in the pore spaces of both media. The tails corresponding to simulated values of u produced by EULAG are larger in both media than the tails associated with ANSYS FLUENT or SSTOKES (Figs. 6a and 10a). This is consistent with observations of generally higher degree of heterogeneity of the state of flow arising from the EULAG-based simulations.

As a general conclusion, these comparisons indicate that the three computational systems produce consistent estimates of the state of flow through explicit natural porous microstructures. This is observed despite the considerable differences among the three solution techniques. The correspondence among the results supports the reliability of employing computational approaches to perform detailed simulations of flow dynamics in complex pore spaces of the kind associated with high definition imaged rock systems which are becoming increasingly available due to the advancement of digital rock physics techniques.

Acknowledgments MS and MR are grateful for partial financial support from MIUR (Project PRIN 2010/2011 "Hydroelectric energy by osmosis in coastal areas"). JDH acknowledges the support of the U.S. Department of Energy through the LANL/LDRD projects 20140002DR (grant no. DE-AC52-06NA25396). PKS acknowledges support by funding received from the European Research Council under the European Union's Seventh Framework Programme (FP7/2012/ERC Grant agreement no. 320375).

References

1. Angot, P., Bruneau, C.H., Fabrie, P.: A penalization method to take into account obstacles in incompressible viscous flows. Numer. Math. **81**, 497–520 (1999)
2. ANSYS Inc.: ANSYS® FLUENT® User's guide, Rel. 12.1 (2009)
3. Barth, T., Jespersen, D.: The design and application of upwind schemes on unstructured meshes. In: 27th Aerospace Sciences Meeting. AIAA Paper 89-0366, Reno (1989)
4. Blunt, M.J., Bijeljic, B., Dong, H., Gharbi, O., Iglauer, S., Mostaghimi, P., Paluszny, A., Pentland, C.: Pore-scale imaging and modeling. Adv. Water Resour. **51**, 197–216 (2013)
5. Blunt, M.J., Jackson, M.D., Piri, M., Valvatne, P.H.: Detailed physics, predictive capabilities and macroscopic consequences for pore-network models of multiphase flow. Adv. Water Resour. **25**, 1069–1089 (2002)
6. Boek, E.S., Venturoli, M.: Lattice-Boltzmann studies of fluid flow in porous media with realistic rock geometries. Comput. Math. Appl. **59**, 2305–2314 (2010)
7. Bourbié, T., Zinszner, B.: Hydraulic and acoustic properties as a function of porosity in Fontainebleau sandstone. J. Geophys. Res. **90**, 11524–11532 (1985)
8. Chen, S., Doolen, G.D.: Lattice Boltzmann method for fluid flows. Annu. Rev. Fluid Mech. **30**(1), 329–364 (1998)
9. Coon, E.T., Porter, M.L., Kang, Q.: Taxila LBM: a parallel, modular lattice Boltzmann framework for simulating pore-scale flow in porous media. Comput. Geosci. **18**, 17–27 (2014)
10. Fourie, W., Said, R., Young, P., Barnes, D.L.: The simulation of pore scale fluid flow with real world geometries obtained from X-ray computed tomography. In: Proceedings of the COMSOL Conference (2007)
11. Gerbaux, O., Buyens, F., Mourzenko, V.V., Memponteil, A., Vabre, A., Thovert, J.F., Adler, P.M.: Transport properties of real metallic foams. J. Colloid Interf. Sci. **342**, 155–165 (2010)
12. Goldstein, D., Handler, R., Sirovich, L.: Modeling a no-slip flow boundary with an external force field. J. Comput. Phys. **105**, 354–366 (1993)
13. Gouze, P., Luquot, L.: X-ray microtomography characterization of porosity, permeability and reactive surface changes during dissolution. J. Contam. Hydrol. **120-121**, 45–55 (2010)
14. Gouze, P., Melean, Y., Le Borgne, T., Dentz, M., Carrera, J.: Non-Fickian dispersion in porous media explained by heterogeneous microscale matrix diffusion. Water Resour. Res. **44**, W11416 (2008)
15. Griebel, M., Klitz, M.: Homogenization and numerical simulation of flow in geometries with textile microstructures. Multiscale Model Sim. **8**(4), 1439–1460 (2010)
16. Guo, Z., Zhao, T.S., Shi, Y.: Preconditioned lattice-Boltzmann method for steady flows. Phys. Rev. E **70**, 066706 (2004)
17. Hyman, J.D., Smolarkiewicz, P.K., Winter, C.L.: Heterogeneities of flow in stochastically generated porous media. Phys. Rev. E **86**, 056701 (2012)
18. Hyman, J.D., Smolarkiewicz, P.K., Winter, C.L.: Pedotransfer functions for permeability: a computational study at pore scales. Water Resour. Res. **49**, 2080–2092 (2013)
19. Hyman, J.D., Winter, C.L.: Hyperbolic regions in flows through three-dimensional pore structures. Phys. Rev. E **88**, 063014 (2013)
20. Hyman, J.D., Winter, C.L.: Stochastic generation of explicit pore structures by thresholding Gaussian random fields. J. Comput. Phys. **277**, 16–31 (2014)
21. Icardi, M., Boccardo, G., Marchisio, D.L., Tosco, T., Sethi, R.: Pore-scale simulation of fluid flow and solute dispersion in three-dimensional porous media. Phys. Rev. E **90**, 013032 (2014)
22. Issa, R.I.: Solution of the implicitly discretized fluid flow equations by operator-splitting. J. Comput. Phys. **62**, 40–65 (1986)
23. Kang, Q., Lichtner, P.C., Zhang, D.: Lattice Boltzmann pore-scale model for multicomponent reactive transport in porous media. J. Geophys. Res. **111**, B05203 (2006)
24. Lopez Penha, D.J., Geurts, B.J., Stolz, S., Nordlund, M.: Computing the apparent permeability of an array of staggered square rods using volume-penalization. Comput. Fluids **51**, 157–173 (2011)
25. Malico, I., Ferreira de Sousa, P.J.S.A.: Modeling the pore level fluid flow in porous media using the immersed boundary method. In: Delgado, J.M.P.Q., et al. (eds.) Numerical Analysis of Heat and Mass Transfer in Porous Media, Advanced Structured Materials, vol. 27, pp. 229–251. Springer, Heidelberg (2012)
26. Manwart, C., Aaltosalmi, U., Koponen, A., Hilfer, R., Timonen, J.: Lattice-Boltzmann and finite-difference simulations for the permeability for three-dimensional porous media. Phys. Rev. E **66**, 016702 (2002)
27. Mittal, R., Iaccarino, G.: Immersed-boundary methods. Ann. Rev. Fluid Mech. **37**, 239–261 (2005)
28. Mostaghimi, P., Blunt, M.J., Bijeljic, B.: Computations of absolute permeability on micro-CT images. Math. Geosci. **45**, 103–125 (2013)
29. Ovaysi, S., Piri, M.: Direct pore-level modeling of incompressible fluid flow in porous media. J. Comput. Phys. **229**(19), 7456–7476 (2010)
30. Pan, C., Hilpert, M., Miller, C.T.: Lattice-Boltzmann simulation of two-phase flow in porous media. Water Resour. Res. **40**, W01501 (2004)

31. Pan, D., Shen, T.T.: Computation of incompressible flows with immersed bodies by a simple ghost cell method. Int. J. Numer. Meth. Fluids **60**, 1378–1401 (2009)
32. Peszynska, M., Trykozko, A.: Pore-to-core simulations of flow with large velocities using continuum models and imaging data. Comput. Geosci. **17**, 623–645 (2013)
33. Prusa, J.M., Smolarkiewicz, P.K., Wyszogrodzki, A.A.: EULAG, a computational model for multiscale flows. Comput. Fluids **37**, 1193–1207 (2008)
34. Raoof, A., Hassanizadeh, S.M.: A new formulation for pore-network modeling of two-phase flow. Water Resour. Res. **48**, W01514 (2012)
35. Sarkar, S., Toksöz, M.N., Burns, D.R.: Fluid flow simulation in fractured reservoirs. Report, Annual Consortium Meeting. MIT Earth Resources Laboratory (2002)
36. Siena, M., Guadagnini, A., Riva, M., Gouze, P., Smolarkiewicz, P.K., Winter, C.L., Hyman, J.D., Inzoli, F., Guédon, G.R., Colombo, E.: A comparison of body-fitted and immersed boundary methods for pore-scale modeling of fully saturated flow in synthetic porous media. In: Hadi, K., Copty, N.K. (eds.) Proceedings of the IAHR International Groundwater Symposium - Modeling and Management Under Uncertainty. Taylor and Francis Group, London (2013)
37. Siena, M., Riva, M., Hyman, J.D., Winter, C.L., Guadagnini, A.: Relationship between pore size and velocity probability distributions in stochastically generated porous media. Phys. Rev. E **89**, 003000 (2014)
38. Smolarkiewicz, P.K.: Multidimensional positive definite advection transport algorithm: an overview. Int. J. Numer. Meth. Fluids **50**, 1123–1144 (2006)
39. Smolarkiewicz, P.K., Margolin, L.G.: MPDATA: a finite-difference solver for geophysical flows. J. Comput. Phys. **140**(2), 459–480 (1998)
40. Smolarkiewicz, P.K., Prusa, J.M.: Forward-in-time differencing for fluids: simulation of geo- physical turbulence. In: Drikakis, D., Geurts, B.J. (eds.) Turbulent Flow Computation, pp. 279–312. Springer, Netherlands (2002)
41. Smolarkiewicz, P.K., Sharman, R., Weil, J., Perry, S.G., Heist, D., Bowker, G.: Building resolving large-eddy simulations and comparison with wind tunnel experiments. J. Comput. Phys. **227**, 633–653 (2007)
42. Smolarkiewicz, P.K., Szmelter, J.: Iterated upwind schemes for gas dynamics. J. Comput. Phys. **228**(1), 33–54 (2009)
43. Smolarkiewicz, P.K., Winter, C.L.: Pore resolving simulation of Darcy flows. J. Comput. Phys. **229**, 3121–3133 (2010)
44. Tartakovsky, A.M., Meakin, P.: A smoothed particle hydrodynamics model for miscible flow in three-dimensional fractures and the two-dimensional Rayleigh–Taylor instability. J. Comput. Phys. **207**(2), 610–624 (2005)
45. Tartakovsky, A.M., Meakin, P., Scheibe, T.D., Eichler West, R.M.: Simulations of reactive transport and precipitation with smoothed particle hydrodynamics. J. Comput. Phys. **222**(2), 654–672 (2007)
46. Tseng, Y.H., Ferziger, J.H.: A ghost-cell immersed boundary method for flow in complex geometry. J. Comput. Phys. **192**, 593–623 (2003)
47. Valvatne, P.H., Blunt, M.J.: Predictive pore-scale modeling of two-phase flow in mixed wet media. Water Resour. Res. **40**, W07406 (2004)
48. Wildenschild, D., Vaz, C.M.P., Rivers, M.L., Rikard, D., Christensen, B.S.B.: Using X-ray computed tomography in hydrology: systems, resolutions and limitations. J. Hydrol. **267**, 285–297 (2002)
49. Zaretskiy, Y., Geiger, S., Sorbie, K., Förster, M.: Efficient flow and transport simulations in reconstructed 3D pore geometries. Adv. Water Resour. **33**, 1508–1516 (2010)